Large nonsaturating magnetoresistance and signature of nondegenerate Dirac nodes in ZrSiS

Ratnadwip Singha[a], Arnab Kumar Pariari[a], Biswarup Satpati[a], and Prabhat Mandal[a,1]

[a]Saha Institute of Nuclear Physics, Homi Bhabha National Institute, Kolkata 700 064, India

Edited by Laura H. Greene, Florida State University, Tallahassee, FL, and approved January 20, 2017 (received for review November 8, 2016)

Whereas the discovery of Dirac- and Weyl-type excitations in electronic systems is a major breakthrough in recent condensed matter physics, finding appropriate materials for fundamental physics and technological applications is an experimental challenge. In all of the reported materials, linear dispersion survives only up to a few hundred millielectronvolts from the Dirac or Weyl nodes. On the other hand, real materials are subject to uncontrolled doping during preparation and thermal effect near room temperature can hinder the rich physics. In ZrSiS, angle-resolved photoemission spectroscopy measurements have shown an unusually robust linear dispersion (up to ∼2 eV) with multiple nondegenerate Dirac nodes. In this context, we present the magnetotransport study on ZrSiS crystal, which represents a large family of materials (*WHM* with *W* = Zr, Hf; *H* = Si, Ge, Sn; *M* = O, S, Se, Te) with identical band topology. Along with extremely large and nonsaturating magnetoresistance (MR), ∼1.4 × 10^5% at 2 K and 9 T, it shows strong anisotropy, depending on the direction of the magnetic field. Quantum oscillation and Hall effect measurements have revealed large hole and small electron Fermi pockets. A nontrivial π Berry phase confirms the Dirac fermionic nature for both types of charge carriers. The long-sought relativistic phenomenon of massless Dirac fermions, known as the Adler–Bell–Jackiw chiral anomaly, has also been observed.

Dirac semimetal | extreme magnetoresistance | chiral anomaly | quantum oscillation | Fermi surface

The discovery of topological insulators (1) and 3D Dirac and Weyl semimetals (2, 3) has emerged as one of the major breakthroughs in condensed matter physics in recent time. Materials with topologically nontrivial band structure serve as a template to explore the quantum dynamics of relativistic particles in low-energy condensed matter systems. In addition to rich physics, these systems offer the possibility of practical applications in magnetic memory, magnetic sensor, or switch and spintronics, due to the novel transport phenomena such as extreme magnetoresistance and ultrahigh mobility (4–6). In Dirac semimetals, bulk valence and conduction bands undergo linear band crossings at fourfold degenerate Dirac points protected by time-reversal symmetry (TRS), inversion symmetry (IS), and crystal symmetry (CS) (7, 8). By breaking either TRS or IS, each Dirac point can be broken into a pair of doubly degenerate Weyl points, accompanied by the surface Fermi arc (7, 8). Theoretical prediction (7, 8) followed by angle-resolved photoemission spectroscopy (ARPES) and transport measurements have verified the existence of bulk Dirac points in Cd_3As_2 and Na_3Bi (2, 9–11) and Weyl nodes in the IS-breaking TX (T = Ta, Nb; X = As, P) family of materials (3, 12–14) and TRS-breaking $YbMnBi_2$ (15). Apart from these compounds, recently, topological nodal line semimetals (TNLSM) have emerged, where the bands cross along one-dimensional closed lines in **k** space instead of discrete points. Although proposed in few materials (16, 17), the existence of the nodal line has been experimentally verified only in IS-breaking noncentrosymmetric superconductor $PbTaSe_2$ (18).

Recently, first-principle calculations and ARPES measurement have revealed the existence of multiple Dirac crossings along with unconventional hybridization of surface and bulk states in ZrSiS (19, 20). The Dirac nodes are protected by nonsymmorphic symmetry and reside at different energy values of band structure with a diamond-shaped Fermi surface. Another feature that makes ZrSiS an interesting system is the energy range of the linear band dispersion. Whereas most of the materials observed so far have linear band dispersion up to a few hundred millielectronvolts from the Dirac point, in ZrSiS the range is observed to be as high as 2 eV in some regions of the Brillouin zone. To realize and exploit the interesting features of Dirac or Weyl fermions in electronic transport properties, the primary requirement is that the Fermi energy of the material should remain within the linear dispersion region. As real materials often undergo uncontrolled doping or deviation from ideal stoichiometry during preparation, very careful and delicate experimental procedures are required to ensure that this primary criterion is fulfilled. On the other hand, the very large energy range of linear band dispersion makes ZrSiS robust enough to satisfy this requirement even when the crystals encounter a certain level of carrier doping or nonstoichiometry. Hence, ZrSiS represents a sturdy topological system, which can be used in industrial applications.

Results

Sample Characterization. High-resolution transmission electron microscopy (HRTEM) and energy-dispersive X-ray (EDX) spectroscopy reveal high quality of the ZrSiS single crystals without any impurity. The details are given in *SI Materials and Methods, SI Sample Characterization* (Figs. S1 and S2).

Significance

Topological semimetals provide the opportunity to explore the fundamental physics of relativistic particles and offer the possibility of technological applications. However, finding robust systems with a sufficiently large range of linearly dispersing bands remains elusive. Recently discovered Dirac semimetal ZrSiS hosts multiple Dirac cones with the largest reported energy range of linear band dispersion (∼2 eV). In this work, we report transport measurements on ZrSiS, exploring extreme and anisotropic magnetoresistance with distinct quantum oscillations, enabling us to quantitatively analyze the Fermi surface properties. We have also observed the unique signature of chiral anomaly in longitudinal magnetoresistance. Our work comprehensively confirms the recent theoretical and angle-resolved photoemission spectroscopy results on ZrSiS and suggests a large family of materials as potential topological semimetals.

Author contributions: B.S. and P.M. designed research; R.S., A.K.P., and B.S. performed research; R.S. and A.K.P. analyzed data; R.S., A.K.P., and P.M. wrote the paper; and P.M. supervised the project.

The authors declare no conflict of interest.

This article is a PNAS Direct Submission.

Freely available online through the PNAS open access option.

[1]To whom correspondence should be addressed. Email: prabhat.mandal@saha.ac.in.

This article contains supporting information online at www.pnas.org/lookup/suppl/doi:10.1073/pnas.1618004114/-/DCSupplemental.

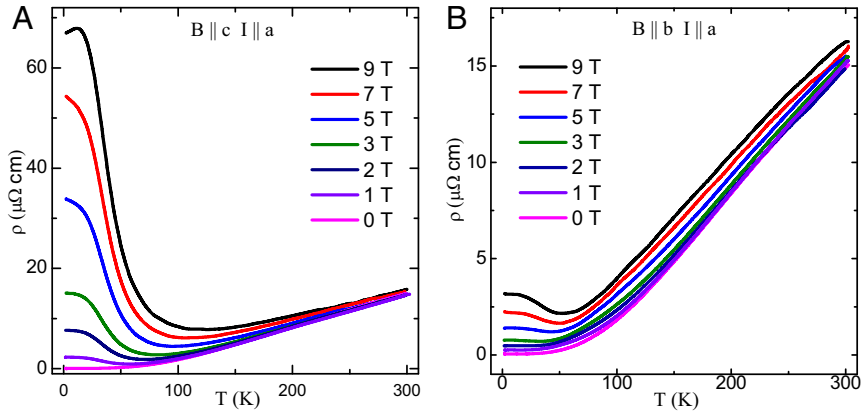

Fig. 1. Temperature dependence of resistivity measured under different transverse magnetic fields. (*A*) ***B*** ∥ **c** axis; (*B*) ***B*** ∥ **b** axis.

Temperature Dependence of Resistivity. As shown in Fig. 1*A*, the zero-field resistivity of ZrSiS shows metallic character. ρ decreases monotonically with the decrease in T down to 2 K. The resistivity at 2 K becomes as low as ∼52 nΩ · cm, which is comparable to that reported for Cd_3As_2 (10). At temperatures below 10 K, the measured resistivity shows some fluctuations within the instrument resolution, which can be explained in terms of the quantum ballistic transport (21). The ultralow residual resistivity and signature of quantum ballistic transport suggest that the mean free path of the charge carriers is very large. Hence, the impurity effect in ZrSiS is almost negligible. The residual resistivity ratio $\rho(300\ \mathrm{K})/\rho(2\ \mathrm{K})$ is found to be 288, which is quite large and confirms good metallicity and high quality of the crystals. The resistivity data, in the temperature range 10–115 K, can be fitted well with the expression $\rho(T) = \rho_0 + AT^n$ with n ∼3, as shown in Fig. S3*A* (*SI Materials and Methods, Magnetotransport Properties*). This indicates a deviation from a pure electronic correlation-dominated scattering mechanism ($n = 2$) (22). A similar type of temperature dependence of ρ has also been observed in unconventional semimetals LaSb ($n = 4$) (23) and LaBi ($n = 3$) (24) and has been attributed to interband electron–phonon scattering. $\rho(T)$ is linear in the high-temperature region above 115 K. With the application of a magnetic field, the low-temperature resistivity undergoes a drastic enhancement, reflecting a metal–semiconductor-like crossover even at a field of 1 T only. This type of magnetic field-induced crossover is often described as a result of gap opening at the band-touching points in topological semimetals (14, 23–26). It is evident from Fig. 1*B* that the metal–semiconductor-like crossover is extremely sensitive to the direction of applied field. With current along the **a** axis and magnetic field parallel to the **c** axis, a strong crossover has been seen. On the other hand, rotating the field direction by 90°, i.e., parallel to the **b** axis, results in much weaker crossover, which occurs at higher field strength. In both the cases, the crossover temperature (T_m) increases monotonically with field and is showing $T_m \propto (B - B_0)^{1/\nu}$-type relation (Fig. S3*B*) (*SI Materials and Methods, Magnetotransport Properties*). ν has a value ∼3 for both the applied field directions and deviates from the value $\nu = 2$ for compensated semimetals Bi, WTe_2, and graphite (27, 28). Considering the thermal activated transport as in the case of intrinsic semiconductor (29), $\rho(T) = \rho_0 exp(E_g/2k_B T)$, we have calculated the values of the thermal activation energy gap ∼20.2 meV and ∼3.7 meV at 9 T, for field directions along the **c** axis and the **b** axis, respectively (Fig. S4 *A* and *B*). The calculated gap E_g shows strong magnetic field dependence (Fig. S4*C*) (*SI Materials and Methods, Magnetotransport Properties*). For both the directions, below T_m, the resistivity exhibits an inflection followed by a plateau region. A similar low-temperature resistivity plateau has been observed in other topological semimetals and is independent of the sample quality (14, 23–26). Therefore, this low-temperature resistivity saturation is an intrinsic property of topological semimetals. However, the origin of this behavior is not yet settled (23).

Extreme Transverse Magnetoresistance. The transverse magnetoresistance (TMR), i.e., the change in resistance with magnetic field applied perpendicular to the current direction, has been measured at several temperatures. As illustrated in Fig. 2*A*, at some representative temperatures, with current parallel to the **a** axis and magnetic field along the **c** axis, an extremely large, nonsaturating magnetoresistance (MR) is obtained. At 2 K and 9 T, MR is 1.4×10^5%, which is comparable to that observed in several Dirac and Weyl semimetals (10, 13, 14, 25, 26). With the increase in temperature, MR decreases dramatically to a value of just about 14% at 300 K and 9 T. At low field, MR shows a

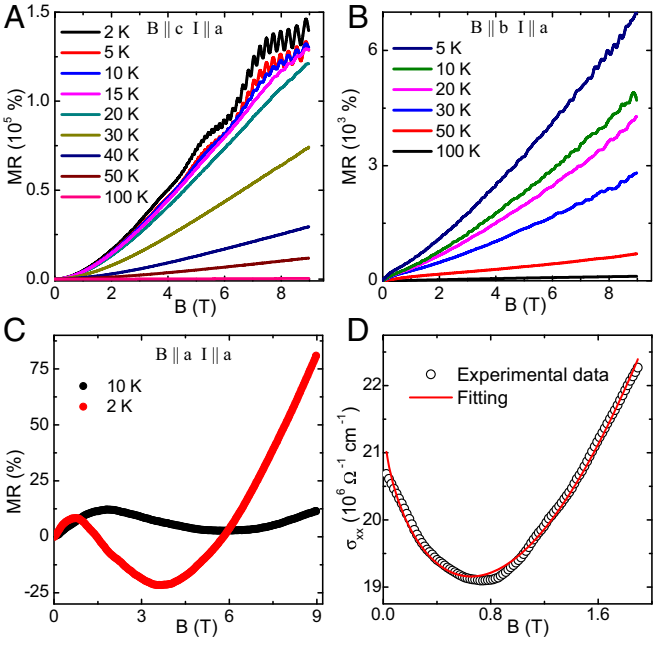

Fig. 2. (*A* and *B*) Transverse magnetoresistance with current along the **a** axis and magnetic field parallel to the (*A*) **c** axis and (*B*) **b** axis, measured at different temperatures, up to 9 T. (*C*) LMR with current and field along the **a** axis. (*D*) Fitting of longitudinal magnetoconductivity data at 2 K, using the semiclassical formula.

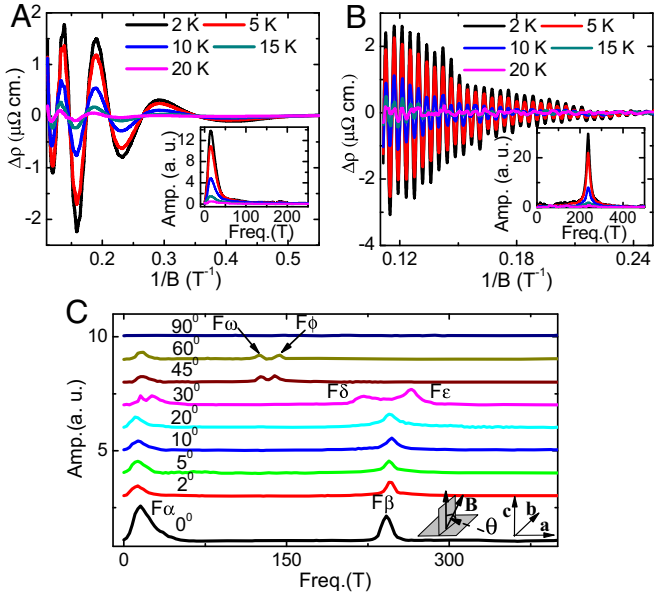

Fig. 3. (*A* and *B*) SdH oscillation obtained by subtracting the smooth background from the MR measurement, plotted with inverse magnetic field (1/*B*) at different temperatures for the two deconvoluted components. *A* and *B*, *Insets* show the corresponding FFT results. (*C*) The angle dependence of oscillation frequencies. For clarity, FFT results for different angles are shifted vertically. The schematic of the experimental setup is shown in *C*, *Inset*.

quadratic field dependence ($\propto B^2$), which becomes almost linear at higher field. As shown in Fig. S4*D* (*SI Materials and Methods, Magnetotransport Properties*), the MR data at different temperatures cannot be rescaled to a single curve, using Kohler's rule $MR = \alpha(\mu_0 H/\rho_0)^m$. The violation of Kohler's rule suggests the presence of more than one type of carrier and/or the different temperature dependence of their mobilities (28, 30). Applying field parallel to the **b** axis and keeping the current direction unchanged, the MR at 9 T has been seen to reduce to ~7,000% at 5 K (Fig. 2*B*). At 3 K and 9 T, the anisotropic ratio $\rho(\boldsymbol{B} \parallel \mathbf{c})/\rho(\boldsymbol{B} \parallel \mathbf{b})$ has a large value of 21, which is comparable to that reported in $NbSb_2$ (26). This result reflects strong anisotropy in electronic structure associated with the quasi-2D nature of the Fermi surface observed in ARPES (20). For a 2D system, where the charge is confined within the plane, the electronic motion is unaffected for the magnetic field parallel to the plane; i.e., the anisotropy in MR will be extremely large. On the other hand, the MR ratio is expected to be close to 1 for an isotropic 3D system.

Longitudinal Magnetoresistance and Chiral Anomaly. Next, the longitudinal MR (LMR) was measured with both the current and magnetic fields applied along the **a** axis. As shown in Fig. 2*C*, negative MR was observed at low field. With the increase in temperature, the negative MR progressively weakens. This negative MR has been ascribed to induced Adler–Bell–Jackiw chiral anomaly in Dirac systems, where a Dirac node splits into two Weyl nodes with opposite chirality due to broken TRS, under application of a magnetic field (8). Parallel magnetic (***B***) and electric (***E***) fields act as a nontrivial gauge field (***E***.***B***), which induces the chiral anomaly, i.e., charge imbalance between the two Weyl nodes of opposite chirality. This causes an extra flow of current along the direction of the applied electric field and results in the negative LMR. The chiral magnetic effect, a long-sought phenomenon proposed in relativistic quantum field theory, has been demonstrated in several 3D Dirac and Weyl semimetals such as Cd_3As_2 (31), Na_3Bi (32), and TaAs (13). The field dependence of longitudinal conductivity [$\sigma_{xx}(B_x)$] at a particular temperature can be analyzed using the semiclassical formula (13),

$$\sigma_{xx}(B_x) = (1 + C_w B_x^2)(\sigma_0 + a\sqrt{B_x}) + (\rho_0 + AB_x^2)^{-1}, \quad [1]$$

where σ_0 and ρ_0 are the zero-field conductivity and resistivity at that temperature, respectively, and C_w is a temperature-dependent parameter originating from chiral anomaly. The term $(\sigma_0 + a\sqrt{B_x})$ takes care of the low-field minima in the conductivity, which is generally described as the effect of weak antilocalization in Dirac systems (13, 32), whereas the second term on the right-hand side includes the contribution from the nonlinear bands near the Fermi level. Fig. 2*D* illustrates the good agreement between the theoretical expression and experimental data. From Fig. 2*C*, it can be seen that the MR becomes positive at high field, which is due to small misalignment of ***E*** and ***B***. The LMR at all temperatures can be well described using a misalignment angle ~2°. The details are provided in *SI Materials and Methods, Magnetotransport Properties* (Fig. S5*A*). We also measured LMR with $\boldsymbol{E} \parallel \boldsymbol{B}$, along different crystallographic directions and on several crystals. For all of the cases, similar negative MR was observed, which confirms that negative LMR is associated with $\boldsymbol{E} \parallel \boldsymbol{B}$ configuration rather than any particular crystallographic direction. In Fig. S5*B*, the measured LMR for the $\boldsymbol{E} \parallel \boldsymbol{B} \parallel \mathbf{b}$ axis is shown as an example. Negative LMR has also been observed in a few systems other than Dirac or Weyl semimetals. However, in these systems the origin and nature of negative MR are completely different from chiral anomaly (*SI Materials and Methods, Magnetotransport Properties*).

SdH Oscillation and Fermi Surface Properties. Another interesting feature that emerges from the transport measurement is the presence of SdH oscillation traceable at fields even below 2 T and temperatures up to 20 K. This not only gives an insight into the nature of the Fermi surface, but also provides evidence of very high mobility of the associated charge carriers. From the TMR data, it is clear that there is more than one frequency. To extract the oscillatory component $\Delta\rho(B)$, a smooth background is subtracted from $\rho(B)$. To deconvolute the two components of oscillation, the background subtraction has been done in two steps.

In Fig. 3 *A* and *B*, $\Delta\rho(B)$, for two different components, is plotted as a function of 1/*B* at several representative temperatures. As the oscillation peaks are very sharp and the field interval used in the measurements is not too small compared with the peak width, some fluctuations in the intensity have been observed in Fig. 3*B*. Using a much smaller field interval, we observed that the peak intensity becomes systematic (Fig. S6*A*). The fast Fourier transform (FFT) analysis of the oscillatory components reveals oscillation frequencies 14 T and 238 T. The obtained frequencies indicate the

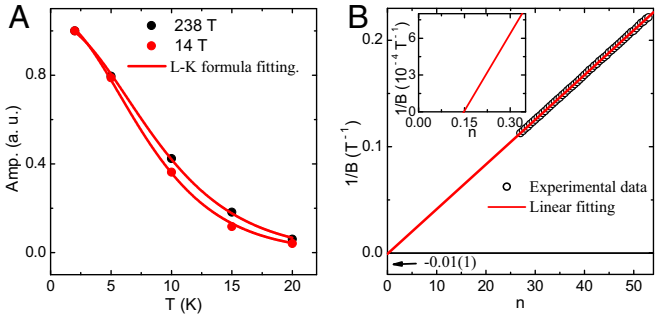

Fig. 4. (*A*) Temperature dependence of relative amplitude of SdH oscillation for both the Fermi pockets. (*B*) Landau-level index plot for 238-T frequency oscillation. *B*, *Inset* shows the *x*-axis intercept by extrapolated linear fitting. Arrow shows the value of the *y*-axis intercept.

existence of a very large and a small Fermi surface cross-section perpendicular to the **c** axis. Using the Onsager relationship, $F = (\varphi_0/2\pi^2)A_F$, where φ_0 is the magnetic flux quantum and A_F is the Fermi surface cross-section perpendicular to the applied magnetic field, we have calculated cross-sections $1.4 \times 10^{-3} \cdot \text{Å}^{-2}$ and $22.7 \times 10^{-3} \cdot \text{Å}^{-2}$ for 14 T and 238 T frequencies, respectively. In Fig. 4*A*, the oscillation amplitude for both the frequencies is shown as a function of temperature and has been fitted using the thermal damping factor of the Lifshitz–Kosevich formula, $R_T = (2\pi^2 k_B T/\beta)/\sinh(2\pi^2 k_B T/\beta)$, where $\beta = e\hbar B/m^*$. From the fitting parameters, the cyclotron effective masses (m^*) of the charge carriers are determined to be $\sim 0.14\, m_0$ and $\sim 0.1\, m_0$ for 238 T and 14 T frequencies, respectively, where m_0 is the rest mass of the free electron. To determine the approximate value of the carrier density, we used its relation with the oscillation frequency (33), $\Delta\left(\frac{1}{B}\right) = \frac{2e}{\hbar}\left(\frac{g_s g_v}{6\pi^2 n_{3D}}\right)^{2/3}$, where g_s and g_v are the spin and valley degeneracies. We found the carrier densities (n_{3D}) to be 2×10^{19} cm^{-3} and 3×10^{17} cm^{-3} for the large and small Fermi pockets, respectively. From the magnetic field-induced damping of oscillation amplitude, $\Delta\rho \propto exp(-2\pi^2 k_B m^* T_D/\hbar eB)$, the Dingle temperatures (T_D) are determined to be 11.2 K and 3.4 K for the large and small Fermi pockets, respectively, at 2 K. To get a quantitative estimate about the mobility of the charge carriers in the system, we calculated the quantum mobility, $\mu_q = (e\hbar/2\pi k_B m^* T_D)$. The obtained values $\sim 1.3 \times 10^3$ cm$^2 \cdot$V$^{-1} \cdot$s^{-1} and $\sim 6.2 \times 10^3$ cm$^2 \cdot$V$^{-1} \cdot$s^{-1} for the large and small frequencies, respectively, imply the significant difference between the mobilities of the carriers, which is expected due to different effective masses of the carriers associated with the Fermi pockets (mobility $\propto \frac{1}{m^*}$). The quantum mobility in a system is always lower than the classical Drude mobility (μ_c), as μ_q is sensitive to both large- and small-angle scattering, whereas μ_c is sensitive to only large-angle scattering (34). The extracted parameters from SdH oscillation are summarized in Table 1. With magnetic field along the **b** axis, no clear oscillation was recorded up to 9 T applied field. This may be due to heavier effective mass and low mobility of the charge carriers along that direction and/or the quasi-2D nature of the Fermi surface in ZrSiS.

Angle Dependence of Oscillation Frequencies. For deeper understanding of the Fermi surface geometry, we performed angle-resolved TMR measurements and SdH oscillation analysis. The resultant FFT spectra for different directions are shown in Fig. 3*C*. Fig. 3*C*, *Inset* illustrates the experimental setup with current along the **a** axis and magnetic field rotated in the **bc** plane. As illustrated in Fig. 3*C*, the low-frequency component F_α (14 T) remains invariant with increasing angle up to 20°, after which it bifurcates into two very closely spaced frequency components. However, with further increase in angle, they come close to each other and merge to become a single frequency. On the other hand, the high-frequency component F_β (238 T) splits into two components (F_δ and F_ε), which are well separated in the frequency spectra. Whereas the higher one (F_ε) among the two disappears above a certain angle, F_δ is seen to shift toward a lower value and then bifurcates (F_ω and F_ϕ). As already discussed,

Table 1. Parameters extracted from SdH oscillation for two Fermi pockets (34)

F	k_F	m^*	v_F	l	μ_q	n_q
T	10^{-2}Å^{-1}	m_0	10^5 m/s	nm	10^3 cm^2/Vs	10^{17} cm^{-3}
238	8.5	0.14	2.4	25.7	1.3	200
14	2	0.1	6.9	247.4	6.2	3

k_F, v_F, and l are the Fermi momentum, Fermi velocity, and mean free path of the charge carriers, respectively.

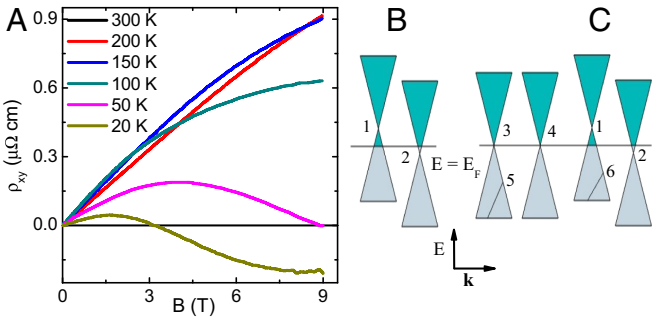

Fig. 5. (*A*) Field dependence of the Hall resistivity measured at different temperatures. (*B*) Schematic explaining transport measurement results. (*C*) Schematic illustrating multiple Dirac cones in ZrSiS as described in earlier reports (19, 20).

with current along the **a** axis and magnetic field along the **b** axis ($\theta = 90°$), no clear oscillatory component was found.

Berry Phase and Zeeman Splitting. In an external magnetic field, a closed orbit is quantized following the Lifshitz–Onsager quantization rule (35), $A_F \frac{\hbar}{eB} = 2\pi(n + \frac{1}{2} - \beta - \delta) = 2\pi(n + \gamma - \delta)$, where $2\pi\beta$ is Berry's phase and δ is a phase shift determined by the dimensionality, having values 0 and $\pm 1/8$ for 2D and 3D cases, respectively. The nature of the electronic band dispersion is determined by the value of the Berry phase, which is 0 for the conventional metals with parabolic band dispersion and π for the Dirac/Weyl-type electronic system with linear band dispersion. The quantity $\gamma - \delta = \frac{1}{2} - \beta - \delta$ can be extracted from the *x*-axis (along which the Landau-level index *n* has been plotted) intercept in the Landau-level fan diagram and takes a value in the range $-1/8$ to $+1/8$ for 3D Dirac fermions (35). In Fig. 4*B*, the Landau-level fan diagram for the larger Fermi pocket in ZrSiS is plotted, assigning maxima of the SdH oscillation as integers (n) and minima as half-integers ($n + 1/2$). Extrapolated linear fitting gives an intercept of 0.15(3) (Fig. 4*B*, *Inset*). The sharp, symmetric, and well-separated oscillation peaks over a wide range ($n = 27$–53) and traceable down to $\sim$4 T imply no significant error in determining the value of the intercept from the linear n vs. $1/B$ fit. On the other hand, with a higher magnetic field to achieve lower Landau level, the nonlinearity in the index plot may arise due to the Zeeman splitting of oscillation peaks as observed for 14-T frequency and discussed below. Similar to that observed for 238-T frequency, a small intercept ~ -0.01 is obtained for 14-T frequency and shown in Fig. S6*B* (*SI Materials and Methods, Magnetotransport Properties*). For both the Fermi pockets, the intercepts are very close to the range $\pm 1/8$. For the smaller frequency, the experimental peak positions are seen to deviate slightly from a straight line that can be attributed to the Zeeman splitting of the Landau levels (34, 36). Although the presence of Zeeman splitting is not clearly visible in the SdH oscillation, the spin–split peaks can be easily distinguished in the de Haas–van Alphen (dHvA) oscillation in our magnetization measurements (Fig. S7 *A* and *B*) (*SI Materials and Methods, Magnetotransport Properties*). Taking the peak and valley positions of the lower-field oscillations, which are almost free from the Zeeman splitting, we also plotted the Landau-level fan diagram for smaller frequency from dHvA oscillation (Fig. S7*C*) and obtained a small intercept, 0.05(2). Furthermore, we calculated Berry's phase from the SdH oscillations at different angles (up to 20°) and did not find any significant change. Finding a reasonably accurate value of Berry's phase for higher angles is much more complicated due to the presence of multiple oscillation frequencies.

Hall Measurement. To determine the nature of the charge carriers of two Fermi pockets, the Hall effect measurement was

performed. At 300 K, the Hall resistivity is found to be almost linear with field and positive (Fig. 5*A*), which indicate holes as majority carriers, consistent with the earlier ARPES report (20). With decreasing temperature, the Hall resistivity develops a sublinear character and at around 50 K it changes sign from positive to negative at high magnetic field, confirming the existence of more than one type of carrier. The overall behavior of the Hall resistivity can be explained by considering low-mobility holes and higher-mobility electrons associated with large and small Fermi pockets, respectively. Following the classical two-band model (37), the Hall resistivity is fitted in Fig. S8 (*SI Materials and Methods, Two-Band Fitting of the Hall Resistivity*). Obtained electron and hole densities, 1.6×10^{17} cm^{-3} and 6×10^{19} cm^{-3}, respectively, are in agreement with those calculated from SdH oscillation. As expected, at 5 K, large electron mobility $\sim 2 \times 10^4$ $cm^2 \cdot V^{-1} \cdot s^{-1}$ and hole mobility $\sim 2.8 \times 10^3$ $cm^2 \cdot V^{-1} \cdot s^{-1}$ have been obtained from the fitted parameters. From the Hall resistivity, it is clear that at least two band crossings are present in the electronic band structure of ZrSiS at different energy values, as shown schematically in Fig. 5*B*. The earlier reports on ARPES and band structure calculations suggest the presence of multiple Dirac crossings at different energy values as illustrated in the schematic in Fig. 5*C*. As shown, the Dirac cones 1 and 2 cross the Fermi energy, having Dirac points at two different energy values. Among the rest, cones 3 and 4 have their band crossing points almost at the chemical potential with negligible Fermi surface, whereas cones 5 and 6 are lying well below the Fermi energy. Thus, in this configuration, it is expected that only Dirac cones 1 and 2 will contribute to the transport properties of ZrSiS, which is consistent with our magnetotransport results.

Summary

In conclusion, we present the systematic study of the magneto-electronic transport properties on ZrSiS single crystals. Magnetic field-induced metal–semiconductor-like crossover along with strongly anisotropic transport properties have been observed. The anisotropic MR along different crystallographic axes is in good agreement with the quasi-2D nature of the Fermi surface observed in ARPES. TMR approaches an extremely large value $\sim 1.4 \times 10^5\%$ at 2 K and 9 T, without any sign of saturation. Under parallel $\boldsymbol{E}$ and $\boldsymbol{B}$ configuration, the observed negative MR implies Adler–Bell–Jackiw chiral anomaly of 3D Dirac fermions in ZrSiS. The SdH oscillation reveals two inequivalent Fermi surface cross-sections perpendicular to the crystallographic **c** axis. The Dirac fermionic nature of the charge carriers is also confirmed from the observed nontrivial π Berry phase in the Landau-level fan diagram for both the Fermi pockets. Nonlinear field dependence of Hall resistivity indicates the presence of both electron- and hole-type charge carriers. Classical two-band fitting of Hall resistivity reveals high mobilities for both types of charge carrier. SdH oscillation along with Hall measurement reflects multiple band crossings at different energy values of the electronic band structure. We believe the present work not only makes a substantive experimental contribution in this contemporary area of research but also can encourage further extensive works in ZrSiS and other members of the family.

During the submission process of our manuscript, several reports on magnetotransport and magnetization measurements in ZrSiS were submitted to arXiv.org (38–40), supporting the major conclusions of our work.

Materials and Methods

The single crystals were grown by a standard iodine vapor transport technique and characterized using HRTEM and EDX spectroscopy. The transport measurements were performed in PPMS (Quantum Design) and a cryogen-free system (Cryogenic) via a four-probe technique. Magnetic measurements were done in MPMS3 (Quantum Design). See *SI Materials and Methods* for details.

ACKNOWLEDGMENTS. We thank N. Khan, A. Paul, and S. Roy for their help during measurements and useful discussions.

1. Hasan MZ, Kane CL (2010) *Colloquium*: Topological insulators. *Rev Mod Phys* 82(4):3045–3067.
2. Liu ZK, et al. (2014) A stable three-dimensional topological Dirac semimetal Cd_3As_2. *Nat Mater* 13(7):677–681.
3. Xu SY, et al. (2015) Discovery of a Weyl fermion semimetal and topological Fermi arcs. *Science* 349(6248):613–617.
4. Daughton JM (1999) GMR applications. *J Magn Magn Mater* 192(2):334–342.
5. Wolf SA, et al. (2001) Spintronics: A spin-based electronics vision for the future. *Science* 294(5546):1488–1495.
6. Lenz J (1990) A review of magnetic sensors. *Proc IEEE* 78(6):973–989.
7. Wang Z, et al. (2012) Dirac semimetal and topological phase transitions in A_3Bi (A=Na, K, Rb). *Phys Rev B* 85(19):195320.
8. Wang Z, Weng H, Wu Q, Dai X, Fang Z. (2013) Three-dimensional Dirac semimetal and quantum transport in Cd_3As_2. *Phys Rev B* 88(12):125427.
9. Neupane M, et al. (2014) Observation of a three-dimensional topological Dirac semimetal phase in high-mobility Cd_3As2. *Nat Commun* 5:3786.
10. Liang T, et al. (2015) Ultrahigh mobility and giant magnetoresistance in the Dirac semimetal Cd_3As2. *Nat Mater* 14(3):280–284.
11. Liu ZK, et al. (2015) Discovery of a three-dimensional topological Dirac semimetal, Na_3Bi. *Science* 343(6173):864–867.
12. Weng H, Fang C, Fang Z, Bernevig BA, Dai X (2015) Weyl semimetal phase in noncentrosymmetric transition-metal monophosphides. *Phys Rev X* 5(1):011029.
13. Huang X, et al. (2015) Observation of the chiral-anomaly-induced negative magnetoresistance in 3d Weyl semimetal TaAs. *Phys Rev X* 5(3):031023.
14. Shekhar C, et al. (2015) Extremely large magnetoresistance and ultrahigh mobility in the topological Weyl semimetal candidate NbP. *Nat Phys* 11(8):645–649.
15. Borisenko S, et al. (2015) Time-reversal symmetry breaking type-II Weyl state in $YbMnBi_2$. arXiv:1507.04847.
16. Kim Y, Wieder BJ, Kane CL, Rappe AM (2015) Dirac line nodes in inversion-symmetric crystals. *Phys Rev Lett* 115(3):036806.
17. Bian G, et al. (2016) Drumhead surface states and topological nodal-line fermions in $TlTaSe_2$. *Phys Rev B* 93(12):121113(R).
18. Bian G, et al. (2016) Topological nodal-line fermions in spin-orbit metal $PbTaSe_2$. *Nat Commun* 7:10556.
19. Xu Q, et al. (2015) Two-dimensional oxide topological insulator with iron-pnictide superconductor LiFeAs structure. *Phys Rev B* 92(20):205310.
20. Schoop LM, et al. (2016) Dirac cone protected by non-symmorphic symmetry and three-dimensional Dirac line node in ZrSiS. *Nat Commun* 7:11696.
21. Zhao Y, et al. (2015) Anisotropic Fermi surface and quantum limit transport in high mobility three-dimensional Dirac semimetal Cd_3As_2. *Phys Rev X* 5(3):031037.
22. Ziman JM (2001) *Electrons and Phonons*, Classics Series (Oxford Univ Press, New York).
23. Tafti FF, Gibson QD, Kushwaha SK, Haldolaarachchige N, Cava RJ (2016) Resistivity plateau and extreme magnetoresistance in LaSb. *Nat Phys* 12(3):272–277.
24. Sun S, Wang Q, Guo PJ, Liu K, Lei H (2016) Large magnetoresistance in LaBi: Origin of field-induced resistivity upturn and plateau in compensated semimetals. arXiv:1601.04618v1.
25. Ali MN, et al. (2014) Large, non-saturating magnetoresistance in WTe_2. *Nature* 514(7521):205–208.
26. Wang K, Graf D, Li L, Wang L, Petrovic C (2014) Anisotropic giant magnetoresistance in $NbSb_2$. *Sci Rep* 4:7328.
27. Kopelevich Y, Pantoja JCM, da Silva RR, Moehlecke S (2006) Universal magnetic-field-driven metal-insulator-metal transformations in graphite and bismuth. *Phys Rev B* 73(16):165128.
28. Wang YL, et al. (2015) Origin of the turn-on temperature behavior in WTe_2. *Phys Rev B* 92(18):180402(R).
29. Hu J, Rosenbaum TF (2008) Classical and quantum routes to linear magnetoresistance. *Nat Mater* 7(9):697–700.
30. McKenzie RH, Qualls JS, Han SY, Brooks JS (1998) Violation of Kohler's rule by the magnetoresistance of a quasi-two-dimensional organic metal. *Phys Rev B* 57(19):11854.
31. Li H, et al. (2016) Negative magnetoresistance in Dirac semimetal Cd_3As_2. *Nat Commun* 7:10301.
32. Xiong J, et al. (2015) Evidence for the chiral anomaly in the Dirac semimetal Na_3Bi. *Science* 350(6259):413–416.
33. Shoenberg D, (1984) *Magnetic Oscillations in Metals* (Cambridge Univ Press, Cambridge, UK).
34. Narayanan A, et al. (2015) Linear magnetoresistance caused by mobility fluctuations in n-doped Cd_3As_2. *Phys Rev Lett* 114(11):117201.
35. Murakawa H, et al. (2013) Detection of Berry's phase in a bulk rashba semiconductor. *Science* 342(6165):1490–1493.
36. Taskin AA, Ando Y (2011) Berry phase of nonideal Dirac fermions in topological insulators. *Phys Rev B* 84(3):035301.
37. Hurd CM (1972) *The Hall Effect in Metals and Alloys* (Plenum, New York).
38. Ali MN, et al. (2016) Butterfly magnetoresistance, quasi-2D Dirac Fermi surfaces, and a topological phase transition in ZrSiS. arXiv:1603.09318v2.
39. Wang X, et al. (2016) Evidence of both surface and bulk Dirac bands in ZrSiS and the unconventional magnetoresistance. arXiv:1604.00108.

40. Hu J, et al. (2016) Evidence of Dirac cones with 3D character probed by dHvA oscillations in nodal-line semimetal ZrSiS. arXiv:1604.01567.
41. Haneveld AK, Jellinek F (1964) Zirconium silicide and germanide chalcogenides preparation and crystal structures. *Recl Trav Chim Pays Bas* 83(8):776–783.
42. Tafti FF, et al. (2016) Temperature-field phase diagram of extreme magnetoresistance. *Proc Natl Acad Sci USA* 113(25):E3475–E3481.
43. Kikugawa N, et al. (2016) Interplanar coupling-dependent magnetoresistivity in high-purity layered metals. *Nat Commun* 7:10903.
44. Ando Y (2013) Topological insulator materials. *J Phys Soc Jpn* 82(10):102001.
45. Huynh KK, Tanabe Y, Tanigaki K (2011) Both electron and hole Dirac cone states in $Ba(FeAs)_2$ confirmed by magnetoresistance. *Phys Rev Lett* 106(21): 217004.